

# Microsize graphene strip grating on gain substrate laser: comparison of the H- and E-polarized mode threshold conditions

FEDIR O. YEVTUSHENKO,<sup>1,\*</sup>  SERGIU V. DUKHOPELNYKOV,<sup>1,2</sup>   
TATIANA L. ZINENKO,<sup>1,3</sup> AND OLEKSANDR I. NOSYCH<sup>1</sup> 

<sup>1</sup>Laboratory of Micro and Nano Optics, Institute of Radio-Physics and Electronics NASU, Kharkiv 61085, Ukraine

<sup>2</sup>Institute of Electronics and Numerical Technologies, Universite de Rennes, Rennes 35042, France

<sup>3</sup>Institute of Electronics and Photonics CAS v.v.i., 18200 Prague 8, Czech Republic

\*fedir.yevtushenko@gmail.com

**Abstract:** We investigate the H- and E-polarized natural modes of infinite flat grating of graphene strips lying on dielectric-slab substrate. The conductivity of graphene is modelled using the quantum-theory Kubo formulas, while the substrate material is assumed to have gain that offsets the radiation and ohmic losses and allows the modes to reach the lasing threshold. We look for the frequency and the gain index threshold value, specific to each mode, as eigenvalues. To find them, we reduce each field problem to a dual series equation for the complex amplitudes of the Floquet spatial harmonics that we analytically regularize based on the inversion of its static part. This results in a Fredholm second-kind infinite determinantal equation for eigenvalues. Increasing the matrix truncation number guarantees the convergence of these quantities to their exact values. Our findings reveal that the lowest thresholds are associated with the lattice modes and that those of the H-polarized plasmon modes can be controlled by graphene's chemical potential within the factor of three.

© 2025 Optica Publishing Group under the terms of the [Optica Open Access Publishing Agreement](#)

## 1. Introduction

Visible and infrared range lasers are various and since recently a promising trend in their development is the use, as working modes, the so-called lattice modes of various periodic arrays [1,2]. Such lasers are able to combine very low emission thresholds and high directionality. Here, the most frequently met configuration is a two-periodic array of noble metal nanoparticles, laying on the flat substrate or embedded into the layer of the gain material [3–9]. As a simpler alternative, one-periodic gratings, i.e., noble metal nanostrip arrays also attract attention [10,11]. It should be noted that in some of these works the lattice modes are incorrectly called the “*lattice plasmon modes*.” In reality, their nature is connected solely to the periodicity – therefore, no surprise that all-dielectric laser designs with the lattice modes are also under active discussion [2,12].

From the experiments, it is visible that finite gratings are able to demonstrate sharp resonances on the lattice modes, and the larger the gratings, the sharper the resonances. This observation is in line with theoretical analyses of the visible light scattering from finite arrays of noble-metal strips and wires [13–15]. To have high Q-factors of such resonances on these arrays, the number of periods in finite grating should be counted in many tens or hundreds.

In the design of the lattice-mode lasers, one can always find the active regions shaped as substrates or superstrates, which contain either internal quantum wells or quantum dot layers or the dye molecules. Experiments show that in the presence of the pumping, the natural modes of such open cavities can be brought to the threshold of the lasing, which can be characterized, from the viewpoint of theory, by the real-valued eigenfrequency.

A usual approach to study the natural modes of the laser cavities has been the classical complex-frequency eigenvalue problem, where the presence of active regions is neglected and considered are the modes of the passive open resonators. This approach is, however, not fully adequate because the existence of the mode-specific threshold gain in the active region is not characterized.

To overcome this deficiency, the introduced in the 2000s Lasing Eigenvalue Problem (LEP) approach takes full account of the active region and uses modified eigenvalues [16–18]. Instead of the complex frequencies, here they are the pairs of the real-valued numbers, the frequency and the material gain index (which is imaginary part of the complex refractive index in the active region). Such a modification is adequate to the lasing because the natural-mode field does not decay in time (stationary emission) and the condition “mode gain = mode losses” is automatically satisfied [16]. This scheme has been applied to microcavity lasers and also to plasmonic nanolasers - silver tube [19] and silver strip [20] in circular quantum wire, and to infinite grating of alternating circular silver and quantum wires [21].

In this work, our goal is to apply the LEP to the accurate analysis of the threshold conditions for the modes of the graphene strip grating on flat substrate made of the gain material (Fig. 1).

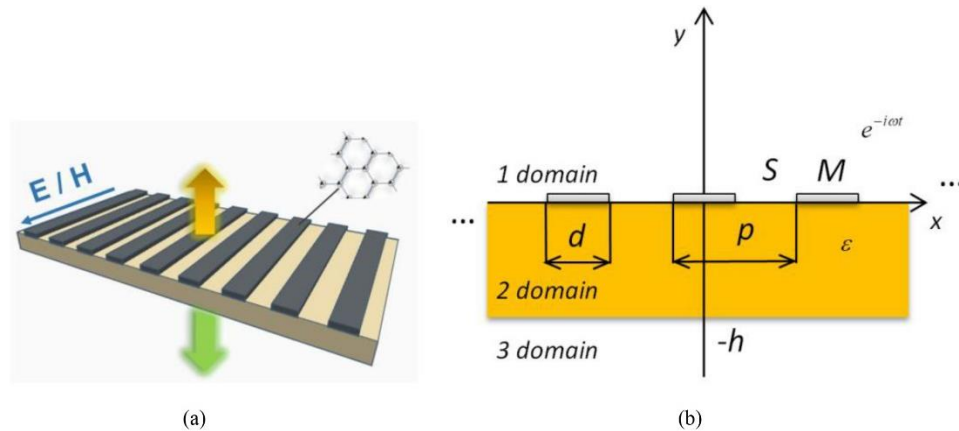


**Fig. 1.** Infinite flat graphene strip grating laying on dielectric substrate (a) and its cross-sectional view with the notations used (b).

As known, graphene has very high electron mobility, tunable by DC bias and characterized by the Kubo approach [22]. Today, this ultrathin material can be controllably patterned into a micro- or nanosize strip gratings using the molecular-beam epitaxial (MBE) technology [23].

Therefore, no surprise that the gratings made of graphene strips or disks placed on or inside dielectric slabs are typical scattering and absorption configurations, which have already important applications in the filtering, sensing, and modulation [24–27]. Theoretical investigations have revealed complicated frequency-selective behavior of such gratings, where the resonances exist on various type modes including the H-polarized plasmon modes of graphene elements. The plasmon-mode frequencies scale down with the size of patterned graphene elements, thus they are found in the infrared if the size is on the nanoscale and in the THz range if it is on the microscale. Additionally, these resonance frequencies can be tuned by changing the chemical potential of graphene that scales with DC bias.

Since the 2020s, graphene plasmons gained attention for building the lasers, although a first vague proposal of such type was published earlier [28]; other potentialities are found in review [29]. More recently spherical-particle and circular-wire laser configurations fully covered with graphene were theoretically considered in [30,31]. Further, the LEPs for a dimer made of two graphene-covered circular quantum wires and for such a wire loaded with centrally placed flat

graphene strip were studied in [32] and [33], respectively. These works have demonstrated that such configurations are composite open resonators, which support natural modes of two families – plasmon modes of graphene covers and dielectric-particle modes of non-graphene elements. The former modes have lower frequencies than the latter ones, and their thresholds are also lower if the cavity size is less than a few micrometers.

The LEP for a graphene strip grating on a substrate can be treated with many techniques; here, the method of analytical regularization [34] occupies special place. We follow [35] and invert the static part of electromagnetic-field problem using, in H-case, the explicit solution of the Riemann-Hilbert Problem (RHP) in the complex calculus and, in E-case, the Inverse Discrete Fourier Transform. The main merit of analytical regularization is the mathematically guaranteed convergence of the final code with progressively larger matrix truncation numbers; additionally, filling in the matrix needs only elementary functions.

This work builds on the preceding short conference papers [36,37], which have been significantly broadened and extended in the details of derivations of the basic equations and in the mode characteristics numerical analysis.

## 2. Casting the eigenvalue problem to determinantal equations, H-case

We consider the 2-D LEP for a harmonic in time ( $e^{-i\omega t}$ , with the cyclic frequency  $\omega$ ) H-polarized electromagnetic field in the configuration presented in Fig. 1. The grating of zero-thickness graphene strips is assumed infinite in  $x$  and lies on the top interface ( $y=0$ ) of the flat dielectric substrate. The strip width is  $d$ , the period is  $p$ , the substrate thickness is  $h$ , and its relative dielectric permittivity is  $\varepsilon = \nu^2 = (\alpha - i\gamma)^2$ . Here, the refractive index  $\alpha$  is assumed known and the gain index  $\gamma > 0$  is unknown. In the H-polarization case, if there is no incident field, we obtain the following boundary value problem for the magnetic field  $z$ -component function,  $H_z(\vec{r}) = H(\vec{r})$ ,  $\vec{r} = (x, y)$ : it has to satisfy (I) 2-D Helmholtz equation inside and outside the substrate, with wavenumbers  $k\nu$  and  $k = \omega/c = 2\pi/\lambda$ , respectively, where  $\lambda$  is the wavelength, and (II) the set of the boundary conditions, which include resistive-sheet boundary conditions at the graphene strips, i.e., at  $\vec{r} \in M : \{y = 0; |x + np| < d/2; n = 0, \pm 1, \dots\}$ ,

$$E_x^{(1)} - E_x^{(2)} = 0, \quad E_x^{(1)} + E_x^{(2)} = 2Z Z_0 [H^{(1)} - H^{(2)}], \quad (1)$$

where  $Z_0 = \sqrt{\mu_0/\varepsilon_0}$  is the free space impedance and the normalized complex-valued graphene surface impedance is,

$$Z(\omega) = Z_0^{-1} (\sigma_{\text{intra}} + \sigma_{\text{inter}})^{-1} \quad (2)$$

Here, the conductivity terms are given by

$$\sigma_{\text{intra}} = \frac{i\Omega Z_0}{\omega + i\tau^{-1}}, \quad \Omega = \frac{q_e^2 k_B T}{\pi \hbar^2 Z_0} \left\{ \frac{\mu_c}{k_B T} + 2 \ln \left[ 1 + \exp \left( -\frac{\mu_c}{k_B T} \right) \right] \right\}, \quad (3)$$

and  $\tau$  is the electron relaxation time,  $q_e$  is the electron charge,  $T$  is the temperature,  $k_B$  is the Boltzmann constant,  $\hbar$  is the reduced Planck constant, and  $\mu_c$  is the chemical potential. The interband term is expressed as integral of known functions, however, has a simple approximation valid if  $\mu_c \gg k_B T$  (at room temperature,  $T = 300$  K,  $k_B T = 0.026$  eV),

$$\sigma_{\text{inter}} = \frac{i q_e^2}{4\pi \hbar} \ln \frac{2\mu_c - (\omega + i\tau^{-1})\hbar}{2\mu_c + (\omega + i\tau^{-1})\hbar} \quad (4)$$

Note that  $|\sigma_{\text{intra}}| \gg |\sigma_{\text{inter}}|$  for the frequencies, lower than certain  $\mu_c$ -dependent value, which lays in the near infrared or visible-light range (see [32]). If the interband term is neglected, then, according to (3),  $\text{Im}Z < 0$  (if the time dependence is chosen as  $e^{-i\omega t}$ ) that is known as inductive impedance behavior - then infinite sheet of graphene can support the propagation of the

plasmon wave [22]. However, close inspection of the Kubo expressions (3) and (4) shows that the imaginary parts of intraband and interband conductivities have opposite signs. Therefore, in principle, at extremely high frequencies where the latter one overweighs the former (see above), the plasmonic nature of graphene gets spoiled.

Besides (1), the tangential field components  $H$  and  $E_x$  have to be continuous across the slots, i.e., at  $\vec{r} \in S : \{y = 0; -\infty < x < +\infty\} \setminus M$ , and across the whole lower interface,  $y = -h$ .

Finally, the function  $H$  has to satisfy (III) the radiation condition, i.e., at  $y \rightarrow \infty$ , it must contain only the outgoing waves, and (IV) the condition of local finiteness of power, which determines the edge behavior of  $H$ : it must tend to zero as a square root of the distance to the strip edges. The conditions (I)-(IV) are inherited from the time-harmonic wave scattering from a passive scatterer (no active region,  $\gamma = 0$ ), with real-valued  $k$ , where they guarantee the uniqueness of the scattered-field function because real  $k$  cannot be an eigenvalue. When studying the LEP for the natural modes of the grating with an active region, we look for the now allowed real-valued  $k$ , therefore, the same conditions are imposed.

From the grating periodicity and Floquet theorem, it follows that the field is a quasi-periodic function of coordinate  $x$ :  $H(x + p, y) = e^{i\beta_0 p} H(x, y)$ , where  $\beta_0$  is the field phase shift on single period (a.k.a. Rayleigh parameter). Therefore, in each domain of Fig. 1 this function can be sought in the form of the Floquet-Rayleigh series of space harmonics,

$$H^{(1)} = \sum_{n=-\infty}^{\infty} a_n e^{i(G_n y + \beta_n x)}, \quad y > 0, \tag{5}$$

$$H^{(2)} = \sum_{n=-\infty}^{\infty} (b_n e^{iG_n^{sl} y} + c_n e^{-iG_n^{sl} y}) e^{i\beta_n x}, \quad 0 > y > -h, \tag{6}$$

$$H^{(3)} = \sum_{n=-\infty}^{\infty} d_n e^{i(-G_n y + \beta_n x)}, \quad y < -h \tag{7}$$

where  $a_n, b_n, c_n, d_n$  are unknown Floquet harmonic amplitudes,  $\beta_n = \beta_0 + 2\pi n/p$ , and the other dimensionless notations are  $G_n = (k^2 - \beta_n^2)^{1/2}$ ,  $G_n^{sl} = (k^2 v^2 - \beta_n^2)^{1/2}$ . Note that the wavenumbers  $k = \pm\beta_n$  (however, not  $k = \pm\beta_n/v$ ) are the field branch-points; they are known as the Rayleigh Anomalies (RAs).

The Rayleigh parameter  $\beta_0$  determines the propagation angle,  $\varphi$ :  $\cos \varphi = \beta_0/k$ , of the 0-th Floquet harmonic with respect to the  $x$ -axis. In the laser experiments, the pumping is usually arranged with a wide beam (flood pumping), so that all periods are in the same conditions. Therefore, we will further assume that  $\beta_0 = 0$ , so that the 0-th harmonic radiates in the normal direction; this restriction, however, is not critical.

To find the mode-specific LEP eigenvalue pairs (frequency and gain index), we substitute Floquet series into the boundary conditions, and reduce this problem to a dual series equation (DSE) for the coefficients  $x_n = g_n a_n / \Gamma_n$ ,

$$\begin{cases} \sum_{n=-\infty}^{\infty} x_n |n| e^{in\phi} = \sum_{n=-\infty}^{\infty} x_n \Delta_n e^{in\phi}, & \theta < |\phi| \leq \pi, \\ \sum_{n=-\infty}^{\infty} x_n e^{in\phi} = 0, & |\phi| < \theta, \end{cases} \tag{8}$$

where

$$\Delta_n = |n| + i(1 + \varepsilon)(\Gamma_n + \kappa Z), \tag{9}$$

$$\Gamma_n = \left[ \frac{1}{g_n} - \frac{\varepsilon}{g_n^{sl}} \frac{(g_n^{sl} - g_n \varepsilon) e^{2ig_n^{sl} \xi} + (g_n^{sl} + g_n \varepsilon)}{(g_n^{sl} - g_n \varepsilon) e^{2ig_n^{sl} \xi} - (g_n^{sl} + g_n \varepsilon)} \right]^{-1}, \tag{10}$$

an  $g_n = (\kappa^2 - n^2)^{1/2}$ ,  $g_n^{sl} = (\kappa^2 \varepsilon - n^2)^{1/2}$ ,  $\kappa = p/\lambda$ ,  $\phi = 2\pi x/p$ ,  $\theta = \pi d/p$ ,  $\xi = 2\pi h/p$ .

The left-hand part of (8) does not depend on the frequency; it forms RHP on the unit circle in the complex plane, solution of which is known and expressed via the Plemelj-Sokhotskii formulas. This allows us to perform analytical regularization of DSE (5), based on the inversion of the static part of the grating in free space problem. All details of this procedure, which makes use of the edge condition, can be found in [34,35].

When applied to (5), this static-part inversion yields an infinite matrix equation,

$$x_m + \sum_{n=-\infty}^{\infty} A_{m,n}x_n = 0, \quad m = 0, \pm 1, \pm 2, \dots \quad (11)$$

$$A_{m,n} = \Delta_n(k, \gamma; \alpha, p, h, \mu_c, \tau)T_{mn}(\theta), \quad (12)$$

where functions  $T_{mn}(\theta)$  are expressed via the Legendre polynomials  $P_m$  of the argument  $u = -\cos \theta$ , see [35,36],

$$T_{mn}(\theta) = \frac{(-1)^{m+n}}{2(m-n)}[P_m(u)P_{n-1}(u) - P_{m-1}(u)P_n(u)], \quad m \neq n, \quad (13)$$

$$T_{00}(\theta) = -\ln \frac{1}{2}(1 + \cos \theta), \quad T_{mm}(\theta) = \frac{1}{2^{|m|}} \left[ 1 + \sum_{s=1}^{|m|} t_s(u)P_{s-1}(u) \right], \quad m \neq 0, \quad (14)$$

$$t_0 = 1, \quad t_1(u) = -u, \quad t_s(u) = P_s(u) - 2uP_{s-1}(u) + P_{s-2}(u) \quad (15)$$

The large-index asymptotics of the Legendre polynomials, together with observation that, if  $n \rightarrow \infty$ , then  $\Delta_n = O(1) + O(e^{-|n|2\pi h/p}) + O(\kappa^2/|n|)$ , allow seeing that

$$\sum_{m,n=-\infty}^{+\infty} |A_{mn}|^2 < \infty, \quad (16)$$

Hence, (11) is a Fredholm second kind matrix equation in the space of sequences  $l_2$ .

Further, by introducing the combinations  $x_n^\pm = x_n \pm x_{-n}$ ,  $n = (0)1, 2, \dots$  and coefficients  $\zeta_0 = 1/2$  and  $\zeta_{n>0} = 1$ , we split both the DSE (5) and the matrix Eq. (11) to two independent equations for the fields, which are symmetric (even) or anti-symmetric (odd), in the coordinate  $x$ , respectively,

$$x_m^\pm + \sum_{n=(0)1}^{\infty} A_{m,n}^\pm x_n^\pm = 0, \quad m = (0), 1, 2, \dots \quad (17)$$

$$A_{m,n}^\pm = \zeta_n \Delta_n(k, \gamma; \alpha, p, h, \mu_c, \tau)[T_{mn}(\theta) \pm T_{-m,n}(\theta)], \quad (18)$$

These matrix equations are also of the Fredholm second kind. Therefore, their infinite-dimension determinants exist as functions of all geometrical and material parameters of the problem. This means that the LEP eigenpairs can be sought for as the characteristic numbers, i.e., the roots of determinantal equations,

$$D^\pm(k, \gamma) = \text{Det} \|\delta_{mn} - \zeta_n \Delta_n(k, \gamma)(T_{mn} \pm T_{-m,n})\|_{m,n=(0)1}^\infty = 0, \quad (19)$$

where  $\delta_{mn}$  is the Kronecker symbol. Then, due to the Fredholm theorems for operator-functions, characteristic numbers of (17) are discrete on the plane  $(k, \gamma)$  and each depends continuously on the problem parameters. Moreover, Fredholm theorems guarantee that the characteristic numbers, found from the truncated determinantal equations for the  $x$ -even and  $x$ -odd modes, converge to the exact values with larger truncation numbers  $N$  [38]. Note that the matrix elements in (17) depend only on the elementary functions and can be quickly computed with arbitrary accuracy.

Still, it is important to see the rate of convergence as it is the rate that determines what value of  $N$  is needed to provide the required accuracy. Therefore, we have defined the error as follows:

$$err(N) = [ |f_N - f_{N+1}|^2 |f_{N+1}|^{-2} + |\gamma_N - \gamma_{N+1}|^2 |\gamma_{N+1}|^{-2} ]^{1/2} \quad (20)$$

and plotted it as a function of  $N$ , for various modes of the considered laser configuration.

Presented further in this paper are the data on the modes of two configurations, the first of which has “wide” strips,  $d = 14 \mu\text{m}$ ,  $p = 70 \mu\text{m}$  (so that  $d/p = 0.2$ ),  $h = 10 \mu\text{m}$ ,  $\mu_c = 0.39 \text{ eV}$ ,  $\tau = 1 \text{ ps}$ . The numerical analysis in this case has been conducted with the truncation number  $N = 50$ . This choice is based on the numerical tests shown in Fig. 2, where the plots illustrate the dependence of the error on the truncation order for the plasmon modes of the graphene strips and the lattice modes (the slab modes errors have similar behavior and are not shown here).

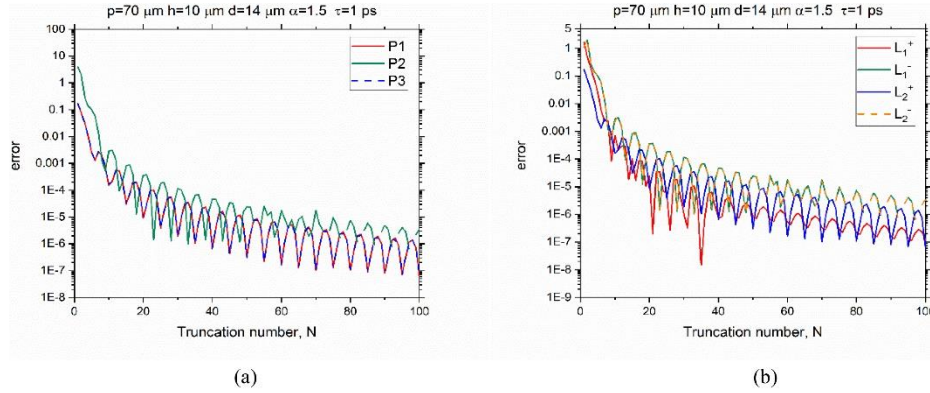


**Fig. 2.** Dependences of the computation error in the LEP eigenpairs for the plasmon modes (a) and the lattice modes (b) on the matrix truncation number, for the parameters as indicated.

As visible,  $N = 50$  ensures at least 5 correct digits in the computed results. Empiric rule for the truncation number that delivers  $D$  correct digits in the computed eigenvalue has been established as  $N = \kappa + p/d + 10D$ .

The second configuration deals with “narrow” strips,  $d = 35 \text{ nm}$ ,  $p = 3 \mu\text{m}$ ,  $h = 10 \mu\text{m}$ ,  $\mu_c = 0.75 \text{ eV}$ ,  $\tau = 1 \text{ ps}$ , and therefore two orders higher frequencies. The main difference, however, is much smaller fill factor  $d/p = 0.0117$ , that entails much lower thresholds of the lattice modes. Therefore, the corresponding eigenvalues have been at first computed with  $N = 50$  and then refined with larger truncation numbers, up to  $N = 800$  for the lattice modes.

### 3. Plasmon, slab and lattice mode frequencies, thresholds and fields, H-case

In Fig. 3(a),(b), we show the color maps of two determinants (19), for  $N = 50$ , as a function of  $f = \omega/2\pi$  and  $\gamma$ . Here, the grating period, strip width and substrate thickness are in the micrometer range,  $p = 70 \mu\text{m}$ ,  $d = 14 \mu\text{m}$ ,  $h = 10 \mu\text{m}$  and  $\alpha = 1.5$ . The minima on the maps host the LEP eigenvalues of the  $x$ -even and  $x$ -odd modes, respectively.

On each map, there is a sequence of modes, which follow a hyperbola,  $f \cdot \gamma = \text{const}$ . These eigenvalues correspond to the plasmon modes of graphene strips. Indeed, following [32,33] and considering graphene strip as a 1-D graphene plasmon surface-wave Fabry-Perot resonator, we obtain their frequencies and associated threshold gain index values as

$$f_m^p \approx \frac{1}{2\pi} \left[ \frac{\pi(m - 0.25)c\Omega}{(\alpha^2 + 1)d} \right]^{1/2}, \quad \gamma_m^p \approx \frac{1}{2\alpha\tau} \left[ \frac{(\alpha^2 + 1)^3 d}{\pi(m - 0.25)c\Omega} \right]^{1/2} \quad (21)$$

where  $m = 1, 2, \dots$  is the mode index and  $\Omega$  is given in (3).

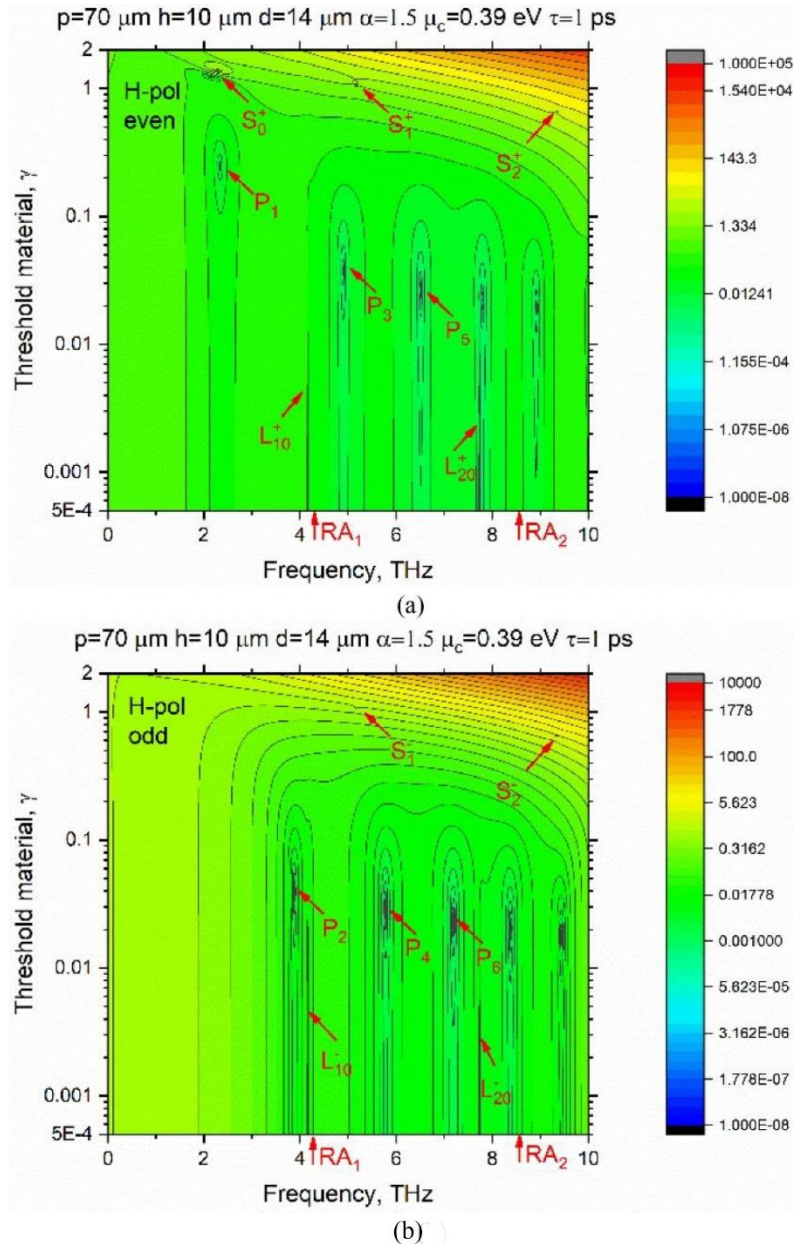


**Fig. 3.** The color maps of the LEP determinants (absolute value) for the  $x$ -even (a) and  $x$ -odd (b) modes of the laser configuration from Fig. 1. The matrix truncation number is  $N = 50$ . Graphene parameters are  $T = 300$  K,  $\tau = 1$  ps, and  $\mu_c = 0.39$  eV. The grating parameters are as indicated.

Note that (21) are derived neglecting the mode radiation losses and the interband contribution (4) to the graphene conductivity. Therefore, these expressions are not accurate at the very low frequencies, where the radiation losses prevail, and very high frequencies (in the visible [32]), where the interband conductivity cannot be neglected. However, between 0.1 and 100 THz they agree with full-wave numerical results [32] and with measurements [23]. The plasmons of the odd indices belong to the class of  $x$ -even modes, and those of the even indices – to the class of  $x$ -odd modes, each class appearing only on one of the maps in Fig. 3.

As one can see from (21), the plasmon-mode frequencies grow and their thresholds drop as  $\sqrt{mc\Omega/d} \approx \sqrt{mc\mu_c/k_B T d}$ , so that indeed  $\gamma_m^P \cdot f_m^P \approx (\alpha^2 + 1)(4\pi\alpha\tau)^{-1}$ . Expressions (21) help estimate the tunability of the plasmon modes under the variation of the chemical potential. If the potential varies from zero to 1 eV, the quantity  $\Omega$  changes approximately tenfold – therefore, both the frequency and the threshold gain change within the factor of 3.

Besides of the plasmon modes, one can see the high-threshold eigenvalues off this hyperbola – they are the lowest slab modes,  $S_{0,1,2}$ , slightly perturbed by the periodic strips. These modes have very large radiation losses hence high thresholds.

Still besides, there are two low-threshold minima on each map, around 4.16 THz and 7.7 THz, which correspond to the lattice modes of the whole grating as a periodic open cavity,  $L_{10}^\pm$  and  $L_{20}^\pm$ , respectively [1,2]. Their emission frequencies are defined primarily by the period of the grating, i.e., are close to the RAs at  $f_m^{RA} = mc/p$ ,  $m = 1, 2, \dots$  (see red arrows at the bottom edge of each map). However, the red shift from RA is defined by the propagation constant of one of the guided natural waves of the dielectric substrate as open waveguide that scales with substrate refractive index  $\alpha$  and thickness  $h$  – see [39] for details. Therefore, each lattice mode has two “parents.” To reflect this circumstance, the first index of the lattice mode, here 1 or 2, corresponds to the nearest RA, i.e., to the 1-st or the 2-nd one. The second index, here 0, corresponds to the index of the principal guided natural wave  $TM_0$  of the dielectric slab, with zero cutoff frequency.

In systematic analysis, we have used the points from the map minima as initial-guess values. As a search algorithm, we used the residual inverse iteration technique (RIIT), details of which can be found in [40], although standard steepest-descent algorithms could be also used. The advantage of RIIT is that it finds the eigenvector together the eigenvalue of the matrix that is needed to build the mode field pattern. More accurate values of the mode emission frequencies and threshold gain index values are presented in Table 1. The Q-factors of the same modes in the passive cavity are estimated by the approximate formula,  $Q = \alpha/\gamma + O(\gamma)$ , derived in [16] (see Eq. (21)), taking into account that the overlap coefficient here equals 1 as the whole volume of the open cavity is the active region.

**Table 1. Wide strip case: H-polarized mode LEP eigenpairs and estimated Q-factors**

$p = 70 \mu\text{m}, h = 10 \mu\text{m}, d = 14 \mu\text{m}, \alpha = 1.5, \mu_c = 0.39 \text{ eV}, \tau = 1 \text{ ps}$			
Mode	Frequency, THz	Threshold gain, $\gamma$	Q-factor, estimation
$P_1$	2.501655	0.152062	9.9
$P_2$	3.881121	0.040944	36.6
$L_{10}^+$	4.165693	0.00424	353.7
$L_{10}^-$	4.162835	0.003903	384.3
$S_0$	2.153888	1.231526	1.1
$S_1^+$	5.176666	1.04789	1.4
$S_1^-$	5.158333	1.083	1.4

The near magnetic-field patterns shown in Fig. 4 and Fig. 5 have been computed for  $N = 50$  and the same graphene and configuration parameters as in Fig. 3. The strip is shown as white

box and the dielectric-air boundaries are shown as black dotted lines. The field patterns support our identification of the plasmon, slab, and lattice modes.

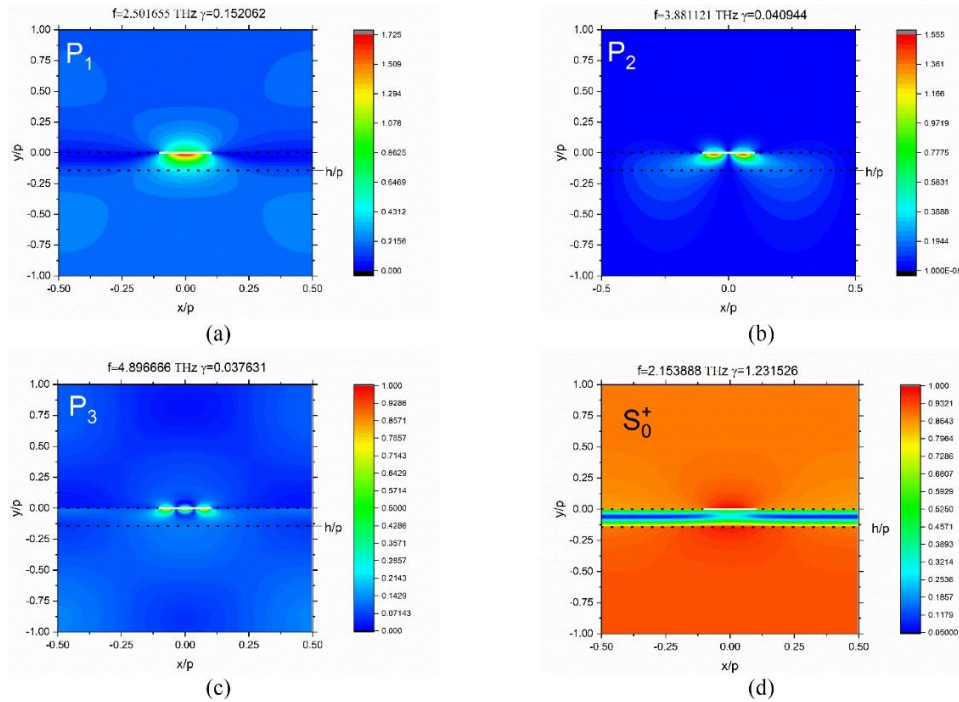


**Fig. 4.** Magnetic field patterns on one period for the plasmon modes  $P_1$ ,  $P_2$ ,  $P_3$  and the slab  $S_0$  mode, for the grating as in Fig. 3.

Note that the plasmon mode magnetic fields stick to the strips and form the bright spots corresponding to the halfwaves of the graphene guided wave. The principal slab mode magnetic field is close to zero at the middle section of the slab (where electric field has maximum – see Fig. 12(a) in Section 5) and deviates from the bare slab mode only in the vicinity of the strips. In contrast, the lattice mode fields form very bright spots that fill the whole slab and stretch out of it, the distance of stretching correlating with the value of the gain threshold index,  $\gamma$  - the smaller the threshold, the further the stretching.

Obviously, a full-wave parametric analysis of the mode emission frequencies and threshold values of the gain index, for all types of modes, is of great importance. First of all, it is interesting to study the role of the chemical potential,  $\mu_c$ . The Fredholm theorems guarantee that each LEP eigenvalue is at least a piece-continuous function of the chemical potential, and the continuity can be spoiled only at the potentials (if they exist) where two eigenvalues coalesce.

However, we have found that the dynamics of the LEP eigenvalues is very complicated. The reason is quite strong dependence of the plasmon-mode frequency and threshold gain on the chemical potential – see (21). As already mentioned, if the potential varies from 0 to 1 eV (this is the largest value accessible today with the best CVD graphene), then the plasmon-mode frequency triples. Indeed, numerical study shows that each plasmon-mode frequency, at some  $\mu_c$ , approaches the frequency of a nearest lattice mode, always lying at the red side of Rayleigh Anomaly, where strong hybridization of the mentioned modes occurs. As an example, in Fig. 6 we present such dependences for the configuration with “wide” strips where all computations can be done with relatively small truncation number,  $N = 50$ .

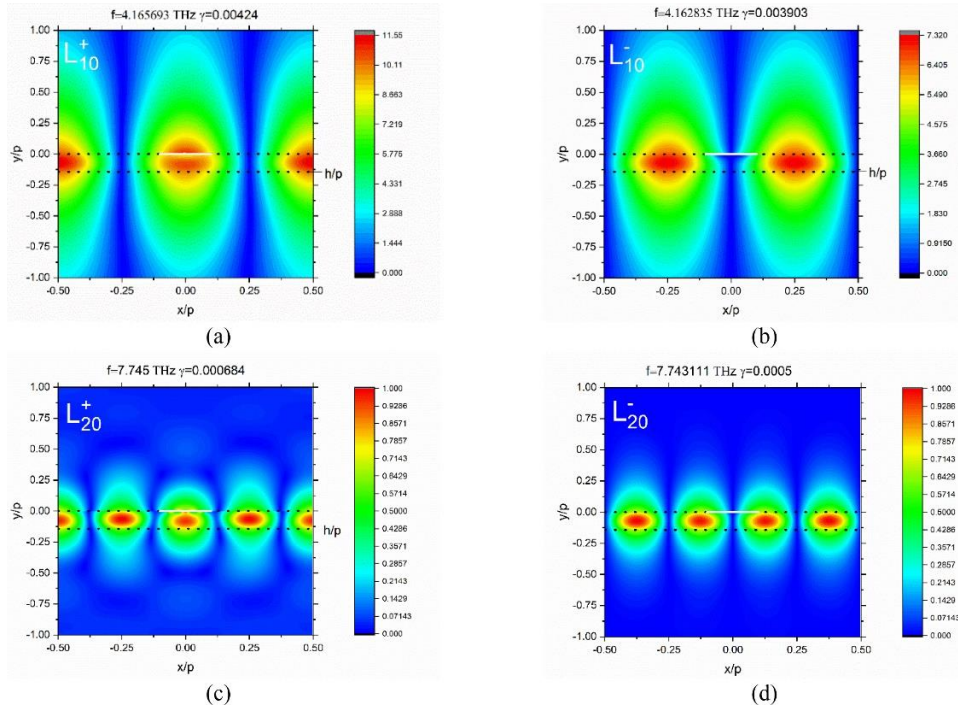


**Fig. 5.** Magnetic field patterns on one period for the lattice modes  $L_{10}^{\pm H}$  and  $L_{20}^{\pm H}$  for the grating as in Fig. 3.

As visible, within each symmetry class of modes, if  $\mu_c$  gets higher, then the plasmon modes show the frequency growth in line with (21) until entering the hybridization regime with a nearest lattice mode, accompanied by the “avoided crossing” of the frequency plots, and the crossing of the threshold gain plots; as known, the mode fields in this regime are the sum and the difference of the partial fields involved, so that the modes “exchange” their field patterns. Therefore, even a consistent notation of any mode becomes a challenge.

Note that, to avoid iterative code jumping from one eigenvalue to another, in the hybridization area the step in parameter (here, potential) variation should be taken appropriately small. We leave, however, a fuller discussion of the mode hybridization details to another publication.

In Fig. 7, we present the color maps of two determinants (absolute value) for the laser with much smaller unit-cell and strip dimensions,  $p = 3 \mu\text{m}$ ,  $d = 35 \text{ nm}$ ,  $h = 1 \mu\text{m}$ , however, larger refractive index,  $\alpha = 1.949$ . The studied frequency band is from 60 THz to 250 THz, i.e., in the infrared range, where the wavelength varies from  $5 \mu\text{m}$  to  $1.2 \mu\text{m}$ .

Note that here the determinant absolute values vary at ultra-small level, from  $10^{-33}$  to  $10^{-40}$  and it is quite difficult to see the minima, which correspond to the eigenvalues. To overcome this difficulty, we started looking for the eigenvalues as the zeros of the other, real-valued quantity – matrix inverse condition number. As known, the condition number is defined as product of the matrix norm and the corresponding inverse matrix norm. As a function of the frequency and threshold index, this quantity varies in much more moderate manner, see the color maps in Fig. 8. At the bottom edge, the red arrows mark the positions of the RAs, which are the branch points, and the black arrows mark the cut-off frequencies of the higher-order guided waves of the substrate.

On these maps, one can see the narrow valleys, which hide the LEP eigenvalues of the high-threshold slab modes, moderate-threshold plasmon modes, and ultralow-threshold lattice modes.

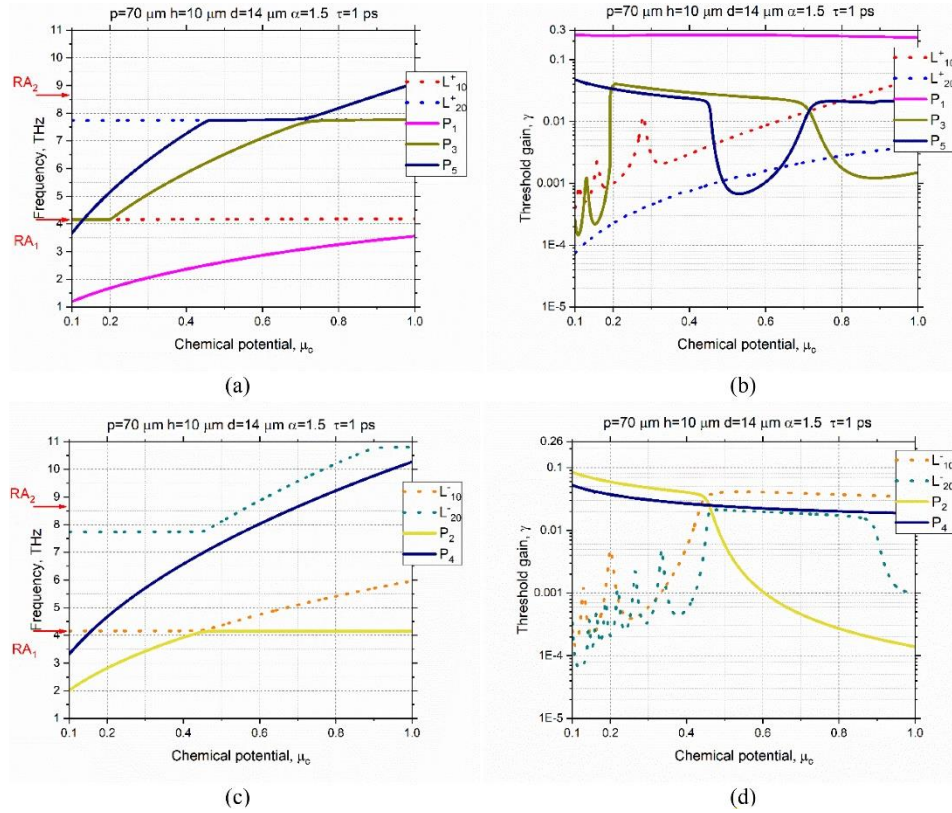


**Fig. 6.** Dependences of the mode emission frequencies (a), (c) and threshold gain indices (b), (d) of the plasmon and the lattice modes of the grating of Fig. 3 on the graphene chemical potential.

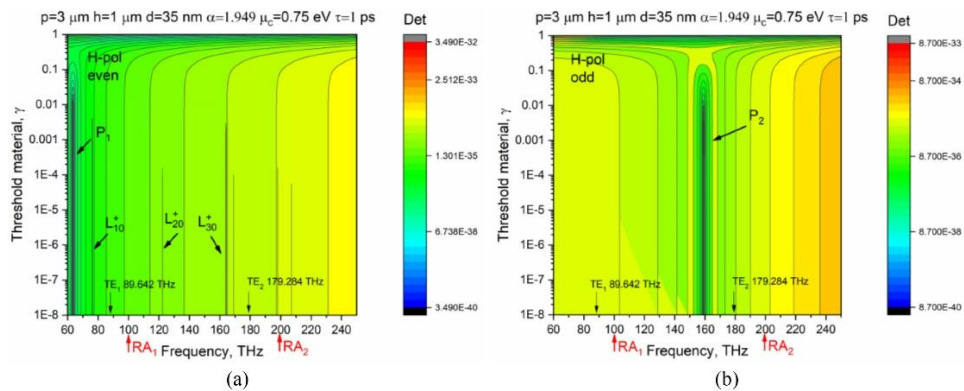


**Fig. 7.** Color maps of the LEP determinants (absolute value) for the  $x$ -even (a) and  $x$ -odd (b) modes of the laser from Fig. 1. The matrix truncation number is  $N = 50$ . Graphene parameters are  $T = 300$  K,  $\tau = 1$  ps, and  $\mu_c = 0.75$  eV. The grating parameters are as indicated.

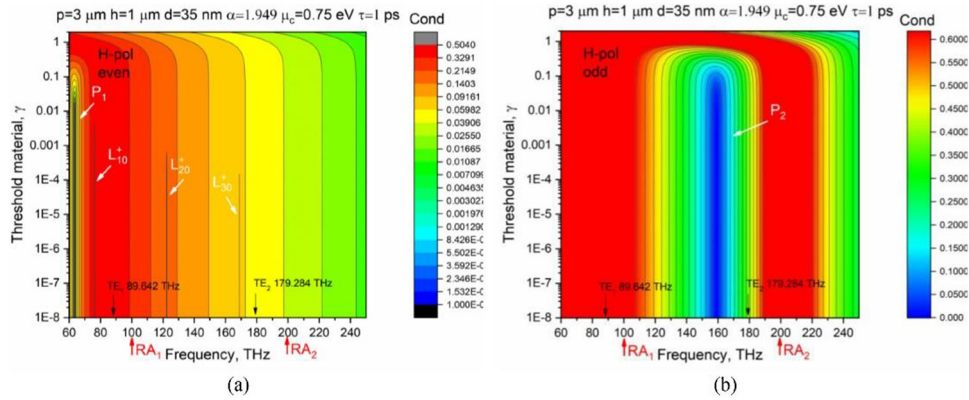


**Fig. 8.** Color maps of the LEP inverse condition number for the  $x$ -even (a) and  $x$ -odd (b) modes of the same laser configuration as in Fig. 7. The matrix truncation number is  $N = 50$ .

Using the maps, we have found these eigenvalues by the iterative RIIT code and then refined with larger  $N$  up to 800; they are presented in Table 2, where symbol ( $\clubsuit$ ) marks still-to-be-refined data.

**Table 2. Narrow strip case: H-polarized mode LEP eigenpairs and estimated Q-factors**

$p = 3 \mu\text{m}, h = 1 \mu\text{m}, d = 35 \text{ nm}, \alpha = 1.949, \mu_c = 0.75 \text{ eV}, \tau = 1 \text{ ps}$			
Mode	Frequency, THz	Threshold gain, $\gamma$	Q-factor, estimated
$P_1^+$	57.9249701561	0.0042844102	454.9
$P_2^-$	88.2878800345	0.002508104	777.1
$L_{10}^+$	76.2285323835	$3.2231874256 \cdot 10^{-6}$	$6.05 \cdot 10^5$
$L_{10}^-$	76.2174034174	$1.3177899938 \cdot 10^{-9}$	$1.48 \cdot 10^9$
$L_{20}^+$	122.2904222966	$2.3425456094 \cdot 10^{-7}$	$8.32 \cdot 10^6$
$L_{20}^-$	122.287012	$5.693 \cdot 10^{-10}$ ( $\clubsuit$ )	$3.4 \cdot 10^9$
$L_{30}^+$	169.032243	$3.46183 \cdot 10^{-8}$ ( $\clubsuit$ )	$5.6 \cdot 10^7$
$L_{30}^-$	169.031012	$5.262 \cdot 10^{-17}$ ( $\clubsuit$ )	$3.7 \cdot 10^{16}$
$S_0$	13.12724260690147	1.86211145744384	1.1

They demonstrate that the  $x$ -odd lattice modes have the thresholds several orders lower than their sister modes of the  $x$ -even class. Some of the modes have extremely low thresholds – for instance, for the  $L_{30}^+$  mode it has the order of  $10^{-8}$ , and for the mode  $L_{30}^-$  it is at the level of machine precision,  $10^{-17}$ .

In Fig. 9, we show the magnetic field of the first plasmon mode,  $P_1$ , and the principal slab mode,  $S_0$ , in the near zone. The strip is shown as white box and the dielectric-air boundaries are shown as black dotted lines. The plasmon mode displays the field, which is tightly bind to the strip, with the number of bright spots corresponding to the mode index. The slab mode displays the magnetic field, which is almost zero at the substrate middle section, similar to the slab without strip where it is exactly zero. Narrow nanostrisps ( $d/p = 0.0117$ ) perturb this pattern, however, very gently.

In Fig. 10, we show the field patterns of the first three lattice modes, of each of two parity classes, created by the 1-st, 2-nd and 3-rd RAs and the principal guided wave of the substrate,  $TM_0$ . As visible, the lattice mode fields are confined inside the slab substrate much better than

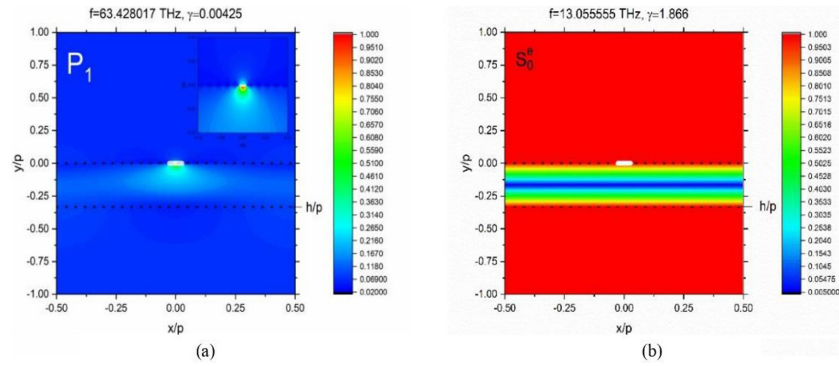


**Fig. 9.** Magnetic field patterns on one period for the  $x$ -even plasmon mode  $P_1$  (a) and the slab mode  $S_0$  (b) for the same grating as in Figs. 7 and 8.

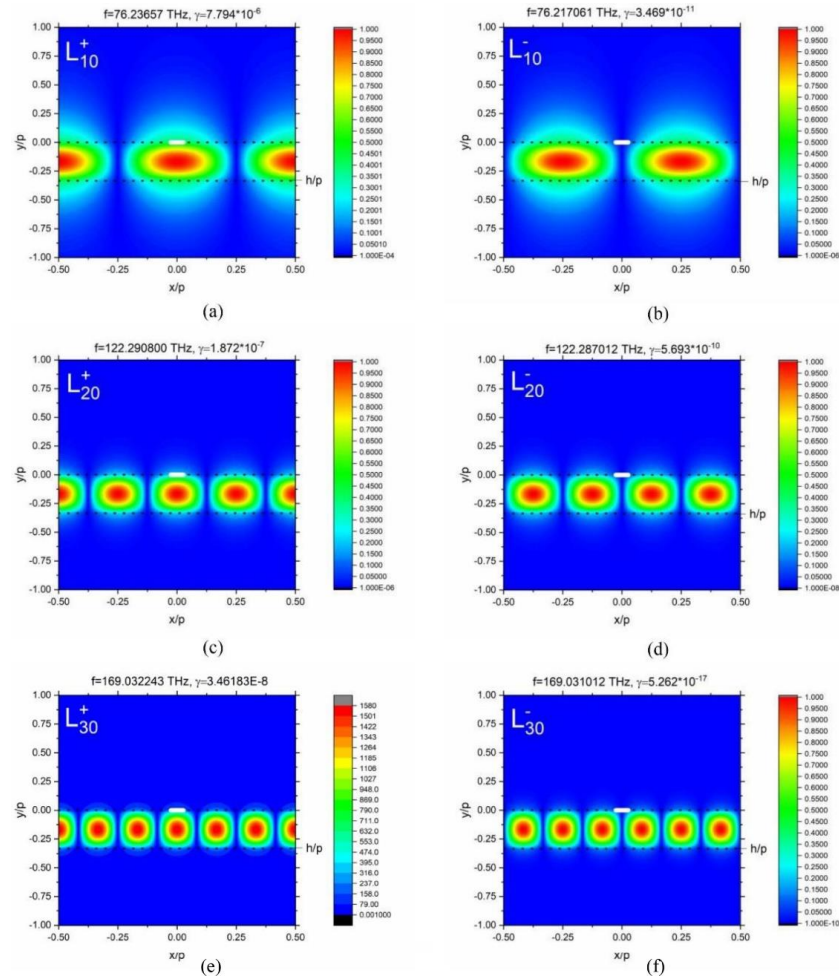


**Fig. 10.** Magnetic field patterns on one period for the  $x$ -even (left column) and  $x$ -odd (right column) lattice modes  $L_{10}^{\pm H}$ ,  $L_{20}^{\pm H}$  and  $L_{30}^{\pm H}$  for the same grating as in Figs. 7–9.

in the case, presented in Fig. 5. This correlates with the several orders lower values of their threshold gain index, which corresponds to smaller ohmic losses in smaller strips and, apparently, smaller radiation losses. As could be expected, the lattice modes of the  $x$ -even and  $x$ -odd parity classes demonstrate very close to each other emission frequencies, however, the  $x$ -odd modes have the lowest values of the threshold gain. This is because here the lossy strips are located at the nearly-zero magnetic field and hence support very weak currents.

The notations in the lattice mode identification,  $L_{mM}^{\pm H}$ , are explained as follows. The field patterns show integer number of bright spots on elementary period ( $2m$ , along the  $x$ -axis) and a single spot across the substrate (along the  $y$ -axis). The first index corresponds to the “parent” RA (and hence the dominant Floquet harmonic number) and the second index corresponds to the “parent” natural wave,  $TM_0$  ( $M=0$ ) guided by the substrate as an open waveguide.

#### 4. Casting the eigenvalue problem to determinantal equations, E-case

In the E-polarization case, the 2-D LEP is formulated similar to the H-case, presented in Section 2. In this case, the basic field component is  $E_z(\vec{r}) = E(\vec{r})$ ,  $\vec{r} = (x, y)$  and the boundary conditions at the strips are

$$E^{(1)} - E^{(2)} = 0, \quad E^{(1)} + E^{(2)} = 2Z Z_0 [H_x^{(1)} - H_x^{(2)}], \quad (22)$$

On expanding  $E(x, y)$  in terms of the Floquet series (5)-(7), substituting them to the boundary conditions, and doing some algebra (all details of which can be found in [39]), the problem is reduced to the following DSE for the unknown coefficients,  $z_n = \delta_{0n} + a_n$ ,

$$\sum_{n=-\infty}^{\infty} z_n \Gamma_n^E e^{in\phi} = \begin{cases} 0, & \theta < |\phi| < \pi, \\ -\frac{\kappa}{Z} \sum_{n=-\infty}^{\infty} z_n e^{in\phi}, & |\phi| < \theta, \end{cases} \quad (23)$$

where

$$\Gamma_n^E = g_n - g_n^{sl} \frac{(g_n^{sl} - g_n) e^{ig_n^{sl}\xi} - (g_n^{sl} + g_n) e^{-ig_n^{sl}\xi}}{(g_n^{sl} - g_n) e^{ig_n^{sl}\xi} + (g_n^{sl} + g_n) e^{-ig_n^{sl}\xi}}, \quad (24)$$

DSE (23) is drastically different from the H-case DSE (8). Its left-hand part can be inverted analytically using the Inverse Discrete Fourier Transform (IDFT) and the orthogonality of the exponents, thus yielding a matrix equation for  $z_n$ . However, the rate of decay of the obtained matrix elements with larger  $|m|$  and  $|n|$  is different. To balance it, we introduce new variables,  $x_n = z_n w_n$ ,  $w_n = (|n| + 1)^{1/2}$ . Finally, combining them as  $x_n^{\pm} = x_n \pm x_{-n}$ ,  $n = (0)1, 2, \dots$ , we split the matrix equation into the  $x$ -even and  $x$ -odd case equations, and arrive at the following result:

$$x_m^{\pm} + \sum_{n=0(1)}^{\infty} A_{mn}^{\pm E} x_n^{\pm} = 0, \quad m = 0(1), \dots, \quad (25)$$

where

$$A_{mn}^{\pm E} = \kappa \zeta_n w_m (Z w_n \Gamma_m^E)^{-1} [S_{mn}(\theta) \pm S_{-m,n}(\theta)], \quad (26)$$

$$S_{mn} = \sin(n - m)\theta / \pi(n - m), \quad S_{mm} = \theta / \pi, \quad (27)$$

$\zeta_0 = 1/2$ ,  $\zeta_{n>0} = 1$ , and  $\theta = \pi d/p$ . Verification of the large-index behavior of the matrix elements  $A_{mn}^{\pm E}$  shows that each of equations (25) is a Fredholm second kind matrix equation in the space of sequences,  $l_2$ . Therefore, the Fredholm theorems guarantee that the characteristic numbers, found from the truncated determinantal equations for the  $x$ -even and  $x$ -odd modes, respectively,

$$D_E^{\pm}(k, \gamma) = \text{Det} \left\| \delta_{mn} + \kappa \zeta_n w_m (Z w_n \Gamma_m^E)^{-1} (S_{mn} \pm S_{-m,n}) \right\|_{m,n=0(1)}^N = 0 \quad (28)$$

converge to the exact values with larger truncation numbers  $N$ . These values, or LEP eigenpairs,  $(k, \gamma)$ , form a discrete set. They can be found by iterations using the minima on the determinant

maps as initial-guess values. Alternatively, the LEP eigenvalues can be searched as zeros of the inverse condition numbers of matrices (25).

## 5. Slab and lattice mode frequencies, thresholds and fields, E-case

In Fig. 11(a),(b), we show two color maps of inverse condition numbers, computed for the E-polarization matrices (25) with  $N = 50$ , as a function of  $f = \omega/2\pi$  and  $\gamma$ . Here, the grating period is  $p = 3 \mu\text{m}$ , strip width is  $d = 35 \text{ nm}$ , substrate thickness is  $h = 1 \mu\text{m}$ ,  $\alpha = 1.949$ , and the graphene parameters are  $\mu_c = 0.75 \text{ eV}$ ,  $\tau = 1 \text{ ps}$ ,  $T = 300 \text{ K}$ . The minima on the maps host the LEP eigenvalues of the  $x$ -even and  $x$ -odd modes, respectively.

These minima are taken as initial-guess values in the iterative search using the RIIT algorithm, as explained in Section 2. The computed values for the LEP eigenpairs, plus the estimations of the corresponding Q-factors, are presented in Table 3.

**Table 3. Narrow strip case: E-polarized mode LEP eigenpairs and estimated Q-factors**

$p = 3 \mu\text{m}, h = 1 \mu\text{m}, d = 35 \text{ nm}, \alpha = 1.949, \mu_c = 0.75 \text{ eV}, \tau = 1 \text{ ps}$			
Mode	Frequency, THz	Threshold gain, $\gamma$	Q-factor, estimated
$L_{10}^+$	64.317705	$6.427 \cdot 10^{-7}$	$3.03 \cdot 10^6$
$L_{10}^-$	64.311292	$2.536 \cdot 10^{-10}$	$7.68 \cdot 10^9$
$L_{11}^+$	97.785096	$5.541 \cdot 10^{-7}$	$3.51 \cdot 10^6$
$L_{11}^-$	97.778700	$6.656 \cdot 10^{-14}$	$2.92 \cdot 10^{13}$
$L_{20}^+$	114.347958	$7.819 \cdot 10^{-8}$	$2.49 \cdot 10^7$
$L_{20}^-$	114.345774	$1.185 \cdot 10^{-10}$	$1.64 \cdot 10^{10}$
$L_{21}^+$	147.153849	$1.329 \cdot 10^{-7}$	$1.46 \cdot 10^7$
$L_{21}^-$	147.149350	$1.865 \cdot 10^{-10}$	$1.05 \cdot 10^{10}$
$L_{22}^+$	192.111694	$9.368 \cdot 10^{-8}$	$2.08 \cdot 10^7$
$L_{22}^-$	192.108106	$1.557 \cdot 10^{-10}$	$1.25 \cdot 10^{10}$
$L_{30}^+$	163.995534	$2.205 \cdot 10^{-8}$	$8.84 \cdot 10^7$
$L_{30}^-$	163.994646	$6.819 \cdot 10^{-11}$	$2.86 \cdot 10^{10}$
$L_{31}^+$	192.638927	$4.157 \cdot 10^{-8}$	$4.69 \cdot 10^7$
$L_{31}^-$	192.636787	$1.523 \cdot 10^{-10}$	$1.28 \cdot 10^{10}$
$S_0$	13.155914	1.857	1.0497
$S_1^+$	85.41519	0.569	3.4259
$S_2^+$	159.29152	0.324	6.0165
$S_3^+$	239.513	0.198	9.8452

One can see several high-threshold eigenvalues – these are the lowest slab modes,  $S_{0,1,2}^\pm$ , which have very large radiation losses. In the E-polarization, there are no plasmon modes. However, there are ultralow-threshold minima on each map, which correspond to the lattice modes of the whole grating as a periodic open cavity, belonging to the  $x$ -even and  $x$ -odd classes.

In Fig. 12, we present the electric-field patterns of two lowest slab modes, slightly perturbed by the strips. Figures 13–15 correspond to the lattice modes computed with  $N = 50$  for the same graphene and configuration parameters as in Fig. 11.

The patterns show integer number of bright field spots on elementary period ( $2m$ , along the  $x$ -axis) and across the substrate ( $M$ , along the  $y$ -axis). The first index corresponds to the “parent” RA (and hence the dominant Floquet harmonic number) and the second index corresponds to the

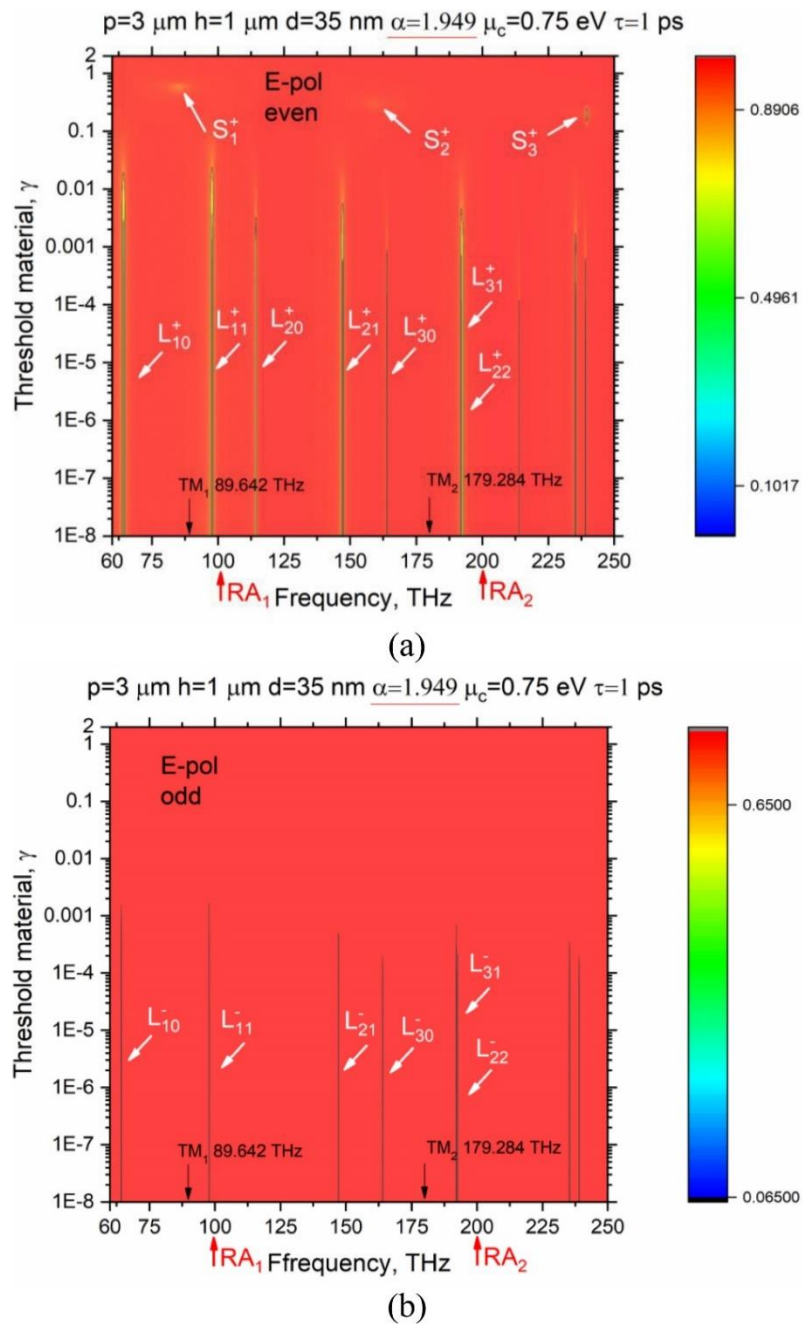


**Fig. 11.** The color maps of the inverse condition number for the  $x$ -even (a) and  $x$ -odd (b) E-polarized modes of the laser in Fig. 1, computed with  $N=50$ . Graphene and grating parameters are  $T=300 \text{ K}$ ,  $\tau=1 \text{ ps}$ ,  $\mu_c=0.75 \text{ eV}$ ,  $p=3 \mu\text{m}$ ,  $d=35 \text{ nm}$ ,  $h=1 \mu\text{m}$ ,  $\alpha=1.949$ .

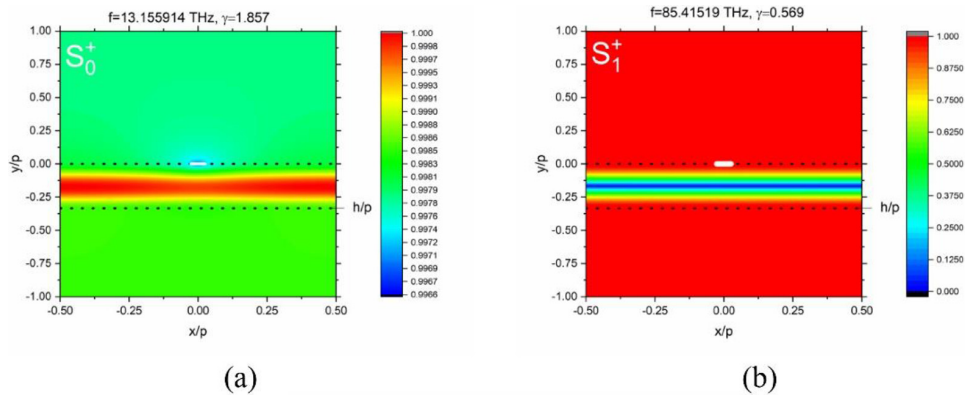


**Fig. 12.** Electric field patterns on one period of the  $x$ -even slab modes  $S_0$  (a) and  $S_1^+$  (b).

“parent” natural wave,  $TE_M$ , ( $M = 0, 1, 2, \dots$ ) guided by the substrate as an open waveguide. This explains our notations in the lattice mode identification,  $L_{mM}^{\pm E}$ .

In Fig. 13, presented are the electric field patterns of the lattice modes, created by the principal guided wave of the substrate,  $TE_0$  ( $M = 0$ ) and the first higher-order wave,  $TE_1$  ( $M = 1$ ), near the 1-st RA. The higher-order wave of the substrate is responsible for the zero field near the median section of the substrate. Note that the  $x$ -even and  $x$ -odd modes of each type have very

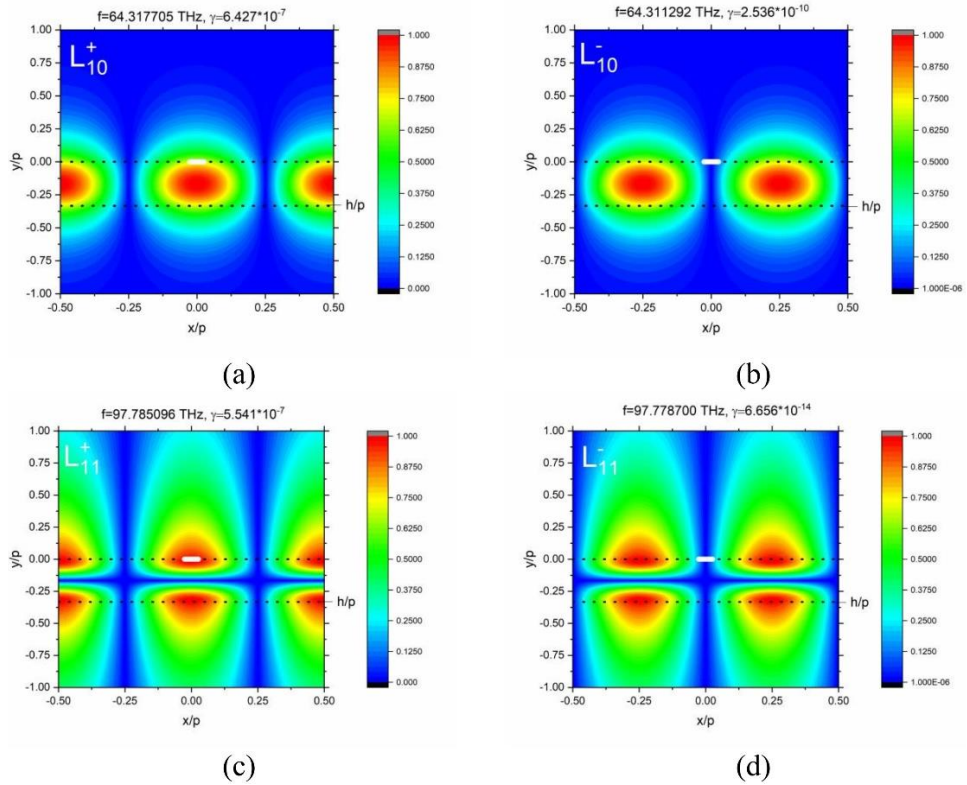


**Fig. 13.** Electric field patterns on one period of the  $x$ -even (left column) and  $x$ -odd (right column) lattice modes,  $L_{10}^{\pm E}$  (top row) and  $L_{11}^{\pm E}$  (bottom row).

similar fields, differing by the shift along the  $x$ -axis by the quarter of period. Their frequencies of emission are also very close to each other – for the  $L_{10}^{\pm E}$  modes they are 64.317705 THz and 64.311292 THz, and for the  $L_{11}^{\pm E}$  modes, they are 97.785096 THz and 97.778700 THz, respectively. However, the threshold gain values are drastically different, for the  $L_{10}^{\pm E}$  modes they are  $10^{-7}$  and  $10^{-10}$ , and for the  $L_{11}^{\pm E}$  modes, they are  $10^{-7}$  and  $10^{-14}$ , respectively. This is because for the  $x$ -even modes the lossy strips are in the E-field maxima, while for the  $x$ -odd they are in the minima.

In Fig. 14, we show the near field patterns for the lattice modes, created by the 2-nd RA and three guided waves of the substrate,  $TE_M$  with  $M = 0, 1$  and 2, i.e.,  $L_{20}^{\pm E}$ ,  $L_{21}^{\pm E}$  and  $L_{22}^{\pm E}$ .

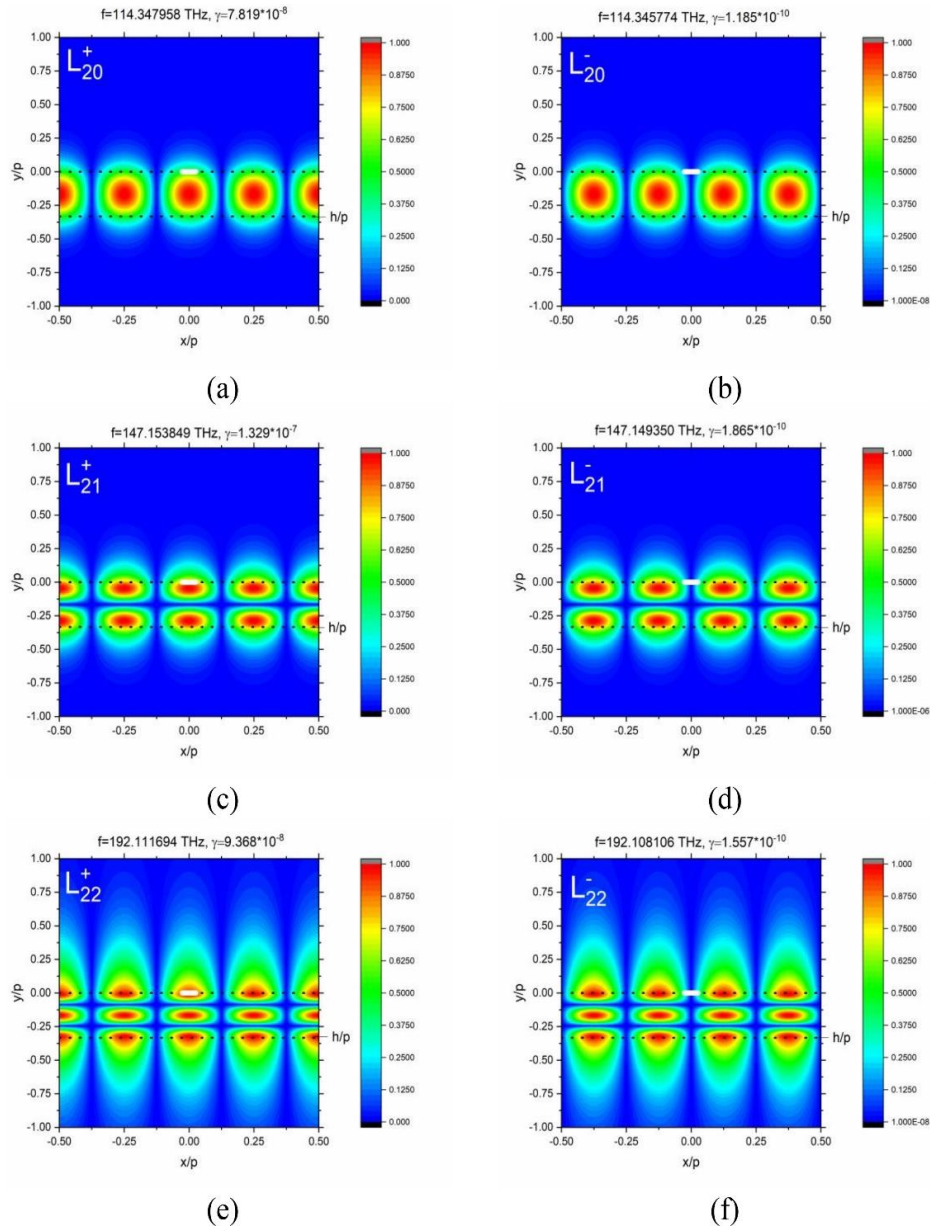


**Fig. 14.** Electric-field patterns on one period for the  $x$ -even (left column) and  $x$ -odd (right column) lattice modes,  $L_{20}^{\pm E}$ ,  $L_{21}^{\pm E}$  and  $L_{22}^{\pm E}$ .

They show the same regularities: the fields (besides of the  $p/8$  shift) and the frequencies of the sister modes of each even-odd doublet are very close to each other, while the gain thresholds are drastically different –  $10^{-8}$  and  $10^{-11}$ , respectively.

Finally, in Fig. 15 we present the near-field patterns for the even-odd doublets of the lattice modes, created by the 3-rd RA and two guided waves of the substrate,  $TE_M$  with  $M = 0$  and  $M = 1$ , i.e.,  $L_{30}^{\pm E}$  and  $L_{31}^{\pm E}$ . They display the same regularities as explained above.

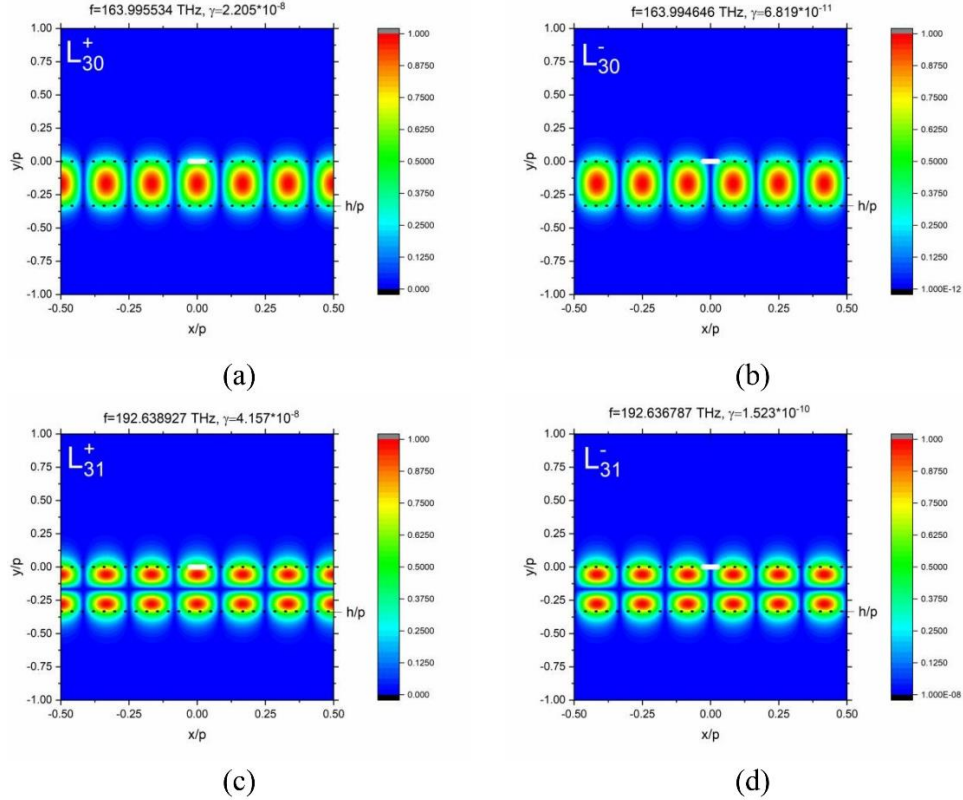


**Fig. 15.** Electric-field patterns on one period for the  $x$ -even (left column) and  $x$ -odd (right column) lattice modes  $L_{30}^{\pm E}$  (upper row) and  $L_{31}^{\pm E}$  (lower row).

## 6. Conclusions

We have considered two mathematical models for the H- and E-polarized natural modes of the laser built on infinite grating of graphene strips on the active (i.e., made of the gain material) substrate, at the threshold of stationary light emission. These models lie entirely in the framework of the classical electromagnetics, however, use a quantum-theory description of the graphene electron conductivity. The corresponding LEPs for the modes of either polarization have been reduced to the determinantal equations for two mode classes of orthogonal parity. Our treatment is based on the analytical inversion of the static part of the problem associated with the grating in free space, with the aid of the RHP technique in H-case and IFDT in E-case. As a result, the matrices, which generate the determinantal equations, are of the Fredholm second kind.

This provides a mathematical proof of the convergence of the characteristic numbers of the truncated determinantal equations to the sought-for LEP eigenvalue pairs, if the matrix truncation order gets larger. Additional and remarkable merit is that the matrix elements depend only on

elementary functions, computable very quickly with superior accuracy. Using the developed algorithms, we have computed the LEP eigenpairs, associated with various H-and E-polarized modes of two laser configurations shaped as graphene-strip grating on the gain substrate, with microsize and nanosize strips, respectively, and discussed their characteristics.

First of all, we have studied the plasmon modes, which exist only in the H-polarization case and found that they are tunable with the aid of the chemical potential of graphene within the factor of 3. This tunability concerns both the frequencies and the threshold gain values. In the main terms, the characteristics of the plasmon modes of the graphene strip grating laser are quite similar to the plasmon modes of the other two configurations, which have been studied with the LEP approach - single and double quantum wires, fully covered with graphene [31,32] and such a wire loaded with a flat graphene strip [33].

However, in the either polarization, the lowest emission thresholds are found for the lattice modes of two possible symmetry classes. These thresholds can be at the level of the machine precision,  $10^{-17}$ , in terms of the gain index, for quite realistic strip, period and substrate parameters – say, 30-nm wide strips of graphene can be found in the sensor reported in [23]. Still, the lattice modes are by no means the so-called “bounded states in continuum” (BICs), which are prohibited by the Optical Theorem.

The above presented results of the LEP analysis, together with the accurate study of the plane-wave scattering from the graphene strip grating on passive dielectric substrate (see [35,39]), convincingly prove that the lattice modes (i) do not have “plasmonic” nature (as frequently believed); instead, they are caused by the periodicity, and (ii) are mediated by the guided waves of the finite dielectric substrate or, in broader sense, the guided waves of the host medium. The periodicity yields the main term in the lattice-mode frequency – this corresponds to the RA frequency. The guided wave yields the main term in the redshift from the RA frequency [39]. In the wave scattering scenario, each lattice mode corresponds to a complex-valued pole of the field as a function of the frequency, with ultra-small imaginary part (i.e., ultrahigh Q-factor). In the lasing condition scenario, each lattice mode has ultralow threshold value of the material gain in the active region.

To the question of possible deviations caused by the finite dimensions of the real-life gratings, a partial answer can be found in the analysis of the plane-wave scattering from finite graphene-strip gratings, suspended in the free space [41]. As visible from plots in Fig. 11 there, the gratings of 50 or more strips, each 20- $\mu\text{m}$  wide and placed with 70- $\mu\text{m}$  period, demonstrate the same per-strip reflectance as infinite strip grating, in the whole THz range except narrow vicinities of RAs. Therefore, today’s graphene-strip grating sensors, which contain many hundred and even thousand strips, display the characteristics that should be even better reproduced by the infinite-grating model. The same can be expected with respect to the mode threshold conditions for the finite-grating laser configurations. Namely, the plasmon-mode and slab-mode thresholds can be expected insensitive to the number of strips, however, the lattice modes should demonstrate the thresholds, which strongly depend on this number until it reaches hundreds or thousands, depending on the configuration.

The zero-thickness model of graphene monolayer is another source of possible deviations from the real-life characteristics. Here, it can be noted that, in fact, the measurements show that graphene usually has a 2-4 nm thickness [23] that points out to the presence of a stack of several monolayers. It is commonly considered that as far as the number of monolayers is small, less than 10, it should be added as a factor to the expressions of the complex conductivity known as the Kubo formalism (3) in order to obtain the conductivity of the stack.

We have performed our analysis assuming that the gain index,  $\gamma$ , is uniform, i.e., not dependent on the frequency, while in reality it is usually characterized by a lorentzian-like spectrum. However, it is easy to see that if the gain is uniform within the interval from  $f_1$  to  $f_2$  and vanishes

off that interval, then all modes that have their frequencies in this interval keep their thresholds the same as above, while the thresholds of the other modes “fly off” to infinity.

**Funding.** National Research Foundation of Ukraine (2020.02.0150).

**Acknowledgments.** V.D. thanks the Programme PAUSE–Solidarity with Ukraine of the Ministry of Higher Education, Research and Innovations, France, the Institute of Electronics and Numerical Technology, University of Rennes, and the Foundation Rennes-Metropole for support. T.L.Z. acknowledges support of the Czech Academy of Sciences via Researches at Risk Fellowship. O.I.N. acknowledges support of the Institute of International Education’s Scholar Rescue Fund. S.V.D., O.I.N. and T.L.Z. are grateful to the Institute of Electronics and Numerical Technologies of the University of Rennes and the Institute of Photonics and Electronics of the Czech Academy of Sciences v.v.i., respectively, for the hospitality.

**Disclosures.** The authors declare no conflicts of interest.

**Data availability.** The authors present the equations, which can be directly programmed with the home-made code that delivers all the results presented.

## References

1. V. O. Byelobrov, T. L. Zinenko, K. Kobayashi, *et al.*, “Periodicity matters: grating or lattice resonances in the scattering by sparse arrays of sub-wavelength strips and wires,” *IEEE Antennas Propag. Mag.* **57**(6), 34–45 (2015).
2. A. D. Utyushev, V. I. Zakomirnyi, and I. L. Rasskazov, “Collective lattice resonances: plasmonics and beyond,” *Rev. Phys.* **6**, 100051 (2021).
3. A. Yang, T. B. Hoang, M. Dridi, *et al.*, “Real-time tunable lasing from plasmonic nanocavity arrays,” *Nat. Commun.* **6**(1), 6939 (2015).
4. M. Ross, C. A. Mirkin, and G. C. Schatz, “Optical properties of one-, two-, and three-dimensional arrays of plasmonic nanostructures,” *J. Phys. Chem. C* **120**(2), 816–830 (2016).
5. J.-P. Martikainen, T. K. Hakala, H. T. Rekola, *et al.*, “Modelling lasing in plasmonic nanoparticle arrays,” *J. Opt.* **18**(2), 024006 (2016).
6. T. B. Hoang, G. M. Akselrod, A. Yang, *et al.*, “Millimeter-scale spatial coherence from a plasmon laser,” *Nano Lett.* **17**(11), 6690–6695 (2017).
7. C. Deeb and J.-L. Pelouard, “Plasmon lasers: coherent nanoscopic light sources,” *Phys. Chem. Chem. Phys.* **19**(44), 29731–29741 (2017).
8. W. Wang, M. Ramezani, A. I. Väkeväinen, *et al.*, “The rich photonic world of plasmonic nanoparticle arrays,” *Mater. Today* **21**(3), 303–314 (2018).
9. R. Li, D. Wang, J. Guan, *et al.*, “Plasmon nanolasing with aluminum nanoparticle arrays,” *J. Opt. Soc. Am. B* **36**(7), E104–E111 (2019).
10. J.-J. Jiang, Y. B. Xie, Z. Y. Liu, *et al.*, “Amplified spontaneous emission via the coupling between Fabry–Perot cavity and surface plasmon polariton modes,” *Opt. Lett.* **39**(8), 2378–2381 (2014).
11. S.-H. Kim, W. S. Han, T.-Y. Jeong, *et al.*, “Broadband surface plasmon lasing in one-dimensional metallic gratings on semiconductor,” *Sci. Rep.* **7**(1), 7907 (2017).
12. K. Xu, M. Fang, and Z. Huang, “Compact unidirectional laser based on all-dielectric metasurface with high quality factor,” *IEEE Photonics J.* **13**(1), 1500109 (2021).
13. O. V. Shapoval and A. I. Nosich, “Finite gratings of many thin silver nanostrips: optical resonances and role of periodicity,” *AIP Adv.* **3**(4), 042120 (2013).
14. D. M. Natarov, R. Sauleau, M. Marciniak, *et al.*, “Effect of periodicity in the resonant scattering of light by finite sparse configurations of many silver nanowires,” *Plasmonics* **9**(2), 389–407 (2014).
15. D. M. Natarov, M. Marciniak, R. Sauleau, *et al.*, “Seeing the order in a mess: optical signature of periodicity in a cloud of plasmonic nanowires,” *Opt. Express* **22**(23), 28190–28198 (2014).
16. E. I. Smotrova, V.O. Byelobrov, T.M. Benson, *et al.*, “Optical theorem helps understand thresholds of lasing in microcavities with active regions,” *IEEE J. Quant. Electron.* **47**(1), 20–30 (2011).
17. V. O. Byelobrov, J. Ctyroky, T.M. Benson, *et al.*, “Low-threshold lasing eigenmodes of an infinite periodic chain of quantum wires,” *Opt. Lett.* **35**(21), 3634–3636 (2010).
18. A. O. Spiridonov, E. M. Karchevskii, T. M. Benson, *et al.*, “Why elliptic microcavity lasers emit light on bow-tie-like modes instead of whispering-gallery-like modes,” *Opt. Commun.* **439**, 112–117 (2019).
19. D. M. Natarov, T. M. Benson, and A. I. Nosich, “Electromagnetic analysis of the lasing thresholds of hybrid plasmon modes of a silver tube nanolaser with active core and active shell,” *Beilstein J. Nanotechnol.* **10**, 294–304 (2019).
20. O. V. Shapoval, K. Kobayashi, and A. I. Nosich, “Electromagnetic engineering of a single-mode nanolaser on a metal plasmonic strip placed into a circular quantum wire,” *IEEE J. Sel. Top. Quant. Electron.* **23**(6), 1501609 (2017).
21. V. O. Byelobrov, T. M. Benson, and A. I. Nosich, “Binary grating of sub-wavelength silver and quantum wires as a photonic-plasmonic lasing platform with nanoscale elements,” *IEEE J. Sel. Top. Quant. Electron.* **18**(6), 1839–1846 (2012).
22. G. W. Hanson, “Dyadic Green’s functions and guided surface waves for a surface conductivity model of graphene,” *J. Appl. Phys.* **103**(6), 064302 (2008).

23. D. Rodrigo, A. Tittl, O. Limaj, *et al.*, “Double-layer graphene for enhanced tunable infrared plasmonics,” *Light: Sci. Appl.* **6**(6), e16277 (2017).
24. M. Jablan, H. Buljan, and M. Soljagic, “Plasmonics in graphene at infrared frequencies,” *Phys. Rev. B* **80**(24), 245435 (2009).
25. M. Kim, S. Kim, and S. Kim, “Ultra-compact integrated terahertz modulator based on a graphene metasurface,” *Opt. Lett.* **46**(3), 605–608 (2021).
26. T. L. Zinenko, A. Matsushima, and A.I. Nosich, “Terahertz range resonances of metasurface based on double grating of microsize graphene strips inside dielectric slab,” *Proc. R. Soc. London, Ser. A* **476**(2240), 20200173 (2020).
27. M. Lucido, M. V. Balaban, and A. I. Nosich, “Terahertz range plasmon and whispering gallery mode resonances in the plane wave scattering from thin microsize dielectric disk with graphene covers,” *Proc. R. Soc. London, Ser. A* **478**(2262), 20220126 (2022).
28. V. Apalkov and M. I. Stockman, “Proposed graphene nanospaser,” *Light: Sci. Appl.* **3**(7), e191 (2014).
29. W. Du, C. Li, J. Sun, *et al.*, “Nanolasers based on 2D materials,” *Laser Photonics Rev.* **14**, 2000271 (2020).
30. M. Cuevas and R. Depine, “Theoretical study of a low-energy spherical core-shell spaser,” *Bienn. Congr. Argentina* (IEEE, 2020).
31. L. Prelat, M. Cuevas, N. Passarelli, *et al.*, “Spaser and optical amplification conditions in graphene-coated active wires,” *J. Opt. Soc. Am. B* **38**(7), 2118–2126 (2021).
32. D. O. Herasymova, S.V. Dukhopelnykov, D.M. Natarov, *et al.*, “Threshold conditions for transversal modes of tunable plasmonic nanolasers shaped as single and twin graphene-covered circular quantum wires,” *Nanotechnology* **33**(49), 495001 (2022).
33. M. E. Kaliberda, S. A. Pogarsky, O. V. Kostenko, *et al.*, “Circular quantum wire symmetrically loaded with a graphene strip as the plasmonic micro/nano laser: threshold conditions analysis,” *Opt. Express* **32**(7), 12213–12227 (2024).
34. T. L. Zinenko, “Scattering and absorption of terahertz waves by a free-standing infinite grating of graphene strips: analytical regularization analysis,” *J. Opt.* **17**(5), 055604 (2015).
35. F. O. Yevtushenko, S. V. Dukhopelnykov, T. L. Zinenko, *et al.*, “Electromagnetic characterisation of tuneable graphene-strips-on-substrate metasurface over entire THz range: analytical regularization and natural-mode resonance interplay,” *IET Microwaves Antenna & Prop* **15**(10), 1225–1239 (2021).
36. F. O. Yevtushenko and S. V. Dukhopelnykov, “Emission frequencies and thresholds for microsize graphene strip grating on gain substrate,” *Proc. European Microwave Conf.* (2023), pp. 548–551.
37. F. O. Yevtushenko, “Threshold analysis for the modes of microsize graphene strip grating laser,” *Proc. Int. Conf. Applied Electromagn. Communic.* (2023), pp. 1–5.
38. O. Karma, “Approximation in eigenvalue problems for holomorphic Fredholm operator function. II. Convergence rate,” *Numeric. Functional Analysis Optim.* **17**(3-4), 389–408 (1996).
39. F.O. Yevtushenko, S.V. Dukhopelnykov, Y.G. Rapoport, *et al.*, “Tunability of non-plasmon resonances in E-polarized terahertz wave scattering from microsize graphene strip-on-substrate grating,” *Opt. Mater. Express* **13**(8), 2274–2287 (2023).
40. A. Neumaier, “Residual inverse iteration for the nonlinear eigenvalueproblem,” *SIAM J. Numeric. Analysis* **22**(5), 914–923 (1985).
41. O.V. Shapoval, J. S. Gomez-Diaz, J. Perruisseau-Carrier, *et al.*, “Integral equation analysis of plane wave scattering by coplanar graphene-strip gratings in the THz range,” *IEEE Trans. Terahertz Sci. Technol.* **3**(5), 666–674 (2013).